NONLINEAR METHODS FOR DEVELOPMENT OF LABEL-FREE HIGH-CONTENT SCREENING INSTRUMENTATION

by

Kent Brasseale

A Thesis

Submitted to the Faculty of Purdue University

In Partial Fulfillment of the Requirements for the degree of

Master of Science

Department of Chemistry

West Lafayette, Indiana

May 2023

THE PURDUE UNIVERSITY GRADUATE SCHOOL

STATEMENT OF COMMITTEE APPROVAL

Dr. Chi Zhang, Chair

Department of Chemistry

Dr. Garth Simpson

Department of Chemistry

Dr. Mike Reppert

Department of Chemistry

Approved by:

Dr. Christine Hrycyna

My wife Sarah and the family I share with her.

ACKNOWLEDGMENTS

First and foremost, I extend my appreciation to Dr. Chi “Jesse” Zhang, my principal investigator, whose brilliance and enthusiasm for microscope research and development set an example to emulate. His experience and patience navigated me through the many times the complexities of nonlinear optics became too much for me to overcome on my own. I will be forever grateful for his devotion of knowledge and time to the progression of my education. It is my deepest desire to maintain and grow the relationship I have with him. I thank him for his hospitality and the time spent within his lab.

I thank my fellow members in the Zhang lab for their support, sharing of ideas, and friendship. I appreciate their eagerness to welcome new students into the fold and to selflessly set time aside for anyone needing help. I hope each of them finds success and happiness in the years to come.

I thank Dr. Garth Simpson, a member of my graduate committee, for his enthusiasm for hard work and learning. I was privileged to experience his teaching on multiple occasions, with each instance influencing me greatly for its ability to instill the importance of learning and creation, rather than simple regurgitation of material. He is an inspirational model for what can be accomplished and created through his commitment to the art and excitement to bring others along.

I thank Dr. Mike Reppert, the final member of my graduate committee, for his investment in my studies and dedication to mentorship. He demonstrated these qualities through the importance he placed on understanding my goals and research while appointed to the committee and by his willingness to set time aside whenever I asked his assistance.

I thank Mike Everly of the Jonathan Amy Facility within the Purdue Chemistry Department for his patience and dedication to the collaboration we had. His expertise was instrumental for the success of the project. His patient explanations helped propel both my education and fascination for the intricacies of image analysis.

I thank my family and friends, both in and out of Purdue, for their continued support and encouragement throughout my pursuits. Their provision of advice and aid has been an undeserving presence through many times of turmoil and indecision. I pray for each of their blessing and that this circle continues to grow throughout my life.

TABLE OF CONTENTS

LIST OF FIGURES

ABSTRACT

Fluorescent labeling and imaging techniques have become a standard for high-content screening (HCS), wherein autonomous spectroscopic imaging leads to detailed information related to multiple biological parameters. However, the chemical labels these fluorescent methods rely on introduce significant challenges to analyzing live cells, such as perturbation to metabolic pathways, poor chemical selectivity, and limited detection channels. Nonlinear spectroscopic methods have historically been incapable of demonstrating competency in high-content screening due to some of the unique qualifications required for sample excitation and signal collection. Nonlinear optical sources of excitation, notably coherent anti-Stokes Raman scattering (CARS), is a rapidly developing field with a label-free nature capable of successfully addressing the shortcomings of fluorescence spectroscopy in many experimental environments, while also presenting unique impediments of its own. Among these are the short working distance incompatible with microplates and the requirement of transmission signal detection to achieve high sensitivity, restricting the application of CARS for HCS. Early attempts to construct the desired HCS pipeline using visible stimulated Raman scattering (SRS) were diverted due to an inability to balance detrimental photodamage with the need for increased energy input to maintain satisfactory signal generation. We developed a label-free CARS HCS platform using a pulse-picking technology and supporting imaging software to image live cells in the epi-direction with high resolution. This configuration allows the use of microplates and a surrounding incubation chamber for precision sample control and the simultaneous label-free chemical analysis of up to 64 conditions. This novel CARS-HCS platform allows automatic quantification and time-lapse monitoring of numerous conditions within a precision-controlled microenvironment.

CHAPTER 1. INTRODUCTION

High content screening (HCS) provides valuable insight into biological systems through the automation of holistic data collection, wherein a sample pipeline is established to facilitate the repeated and simultaneous measurement of multiple parameters in complex samples to determine phenotypic responses. HCS has become a mainstay in metabolic research and drug discovery due to its ability to target specific molecules in the biological system and return their effects on the numerous pathways they interact with[1,2]. As a versatile exploratory tool, HCS is able to unearth if subpopulations within a cell line exist and if they respond differently to a given stimulus, how drug treatments can be fine-tuned to direct a biological response, and how metabolites are managed within a system. An HCS platform is fundamentally composed of the instrumentation required to facilitate signal generation and collection of samples in rapid succession and the accompanying software for control of the imaging parameters. For this purpose, fluorescent labeling-based methods have increasingly risen in popularity for their well-researched application in a plethora of biological systems and ease of signal detection[1,3]. Limitations of current fluorescent labeling techniques in the form of perturbation to metabolic pathways, poor chemical selectivity, and limited detection channels have seen researchers begin experimenting with other sources for spectroscopic data collection to supplant fluorescence in HCS.

Nonlinear approaches have become contenders for this purpose, with stimulated Raman scattering (SRS) and coherent anti-Stokes Raman scattering (CARS) each being strong candidates in this category for the rich molecular vibrational transition information provided[4,5,6,7]. The Jablonski diagrams found in Figure 1.1 illustrate the differences between the Raman techniques[8]. Both SRS and CARS find origins in spontaneous Raman (SR), where an incident photon has a small probability to provoke an inelastic scattering event which subsides in an energy change of the photon equal to the vibrational transition where the event originated[7]. However, a low scattering cross-section makes single image acquisition times for SR 10 or more hours, making it incompatible with the premise of HCS platforms, to analyze the sample environment in real-time. SRS and CARS each rely on multi-photon processes to increase the reliability of producing the desired energy-shifted photon by inducing resonance of a vibrational transition.

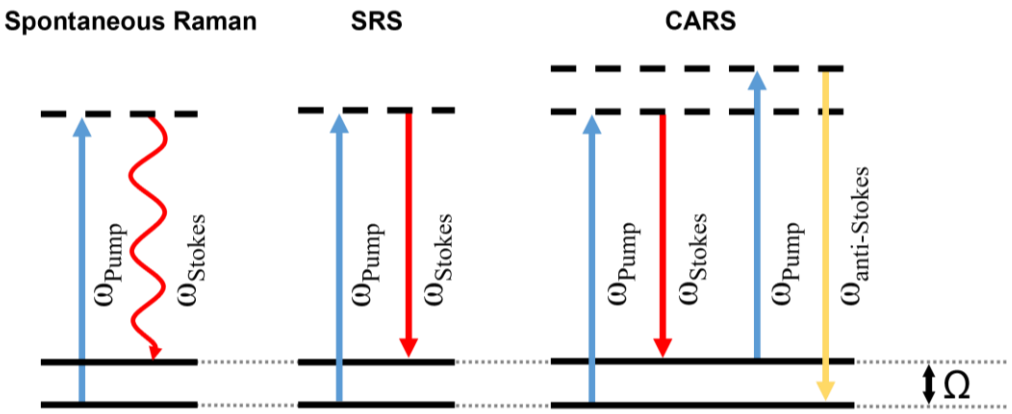

Figure 1.1. Jablonski diagrams of spontaneous Raman, SRS, and CARS, with the latter two noteworthy as multi-photon, resonance enhanced methods for obtaining information on the vibrational transitions of molecules within the sample[8].

Despite their label-free nature and high chemical selectivity, SRS and CARS present unique impediments of their own for HCS platforms. The most critical barrier is caused by the input pulse being the coherent carrier of SRS signals and the forward-CARS signal being substantially stronger than the epi-CARS[6,9]. In both cases, this necessitates signal detection be in the forward direction for transparent samples to achieve practical image quality. High numerical aperture (NA) objective lenses and condensers, which have very short working distances, are enlisted to focus the high energy beams required for these nonlinear processes and collect the resulting forward direction signal, respectively[7]. To date, the inability to insert the required hardware for HCS operation in the limited forward direction working distance and poor signal generation in the epi direction has prevented the demonstration of a nonlinear HCS platform, despite the rapid advancements to SRS and CARS that have been implemented in recent years. However, careful manipulation of the incident beam's properties may allow researchers to bypass these pitfalls.

We constructed a hyperspectral label-free visible SRS HCS platform through frequency doubling the excitation pulses to allow the use of a lower NA objective lens and incorporated a 1D galvanometer for micro-delay adjustments of the stokes beam for hyperspectral imaging. This innovation increases the working distance post objective for incorporation of a micro-well plate and incubation chamber for HCS and maintains high sensitivity and resolution. The original purpose of the instrument was to monitor cell metabolites and/or exogenous chemical introductions through leveraging the high chemical selectivity and resolution SRS offers; however,

we found thar SRS signal are much weaker when low NA objectives with long working distances are used despite using shorter wavelength pulses for excitation. The frequency doubling of the excitation pulses coincides with the doubling of the same beams' energies. When a high NA objective is used, coupled with the tight focus of the electric field required to produce significant amounts of the coherent signal, this energy increase resulted in rapid degradation throughout the biological samples from photodamage. Subsequent efforts to balance the input energy with desired signal generation levels proved unsuccessful.

Despite this setback, the SRS apparatus for HCS is functional and plans for its application have been amended for use in the measurement of crystalline properties of samples at low wavenumbers. These crystal-like samples are not susceptible to photodamage in the same manner as biological samples and the information gained from SRS at low wavenumbers provides insight into its ordering, purity, and composition[10,11,12]. The HCS capabilities of the platform further support its use for this research because many industries, such as in semiconductor fabrication, desire rapid analysis of many sets of spectral data at high resolution for quality control purposes[11,12]. We therefore intend to transition the innovated SRS HCS platform into performing spectral data collection and analysis of crystalline samples to determine lattice properties.

To conserve our intentions for the platform to be an HCS tool for biological sample analysis, we incorporated a Pulse-Picking CARS (PP-CARS) line which mitigates the appearance of photodamage without forcing compromises on imaging quality. This novel pulse-picking technology employs an acoustic-optic modulator to control the duty cycle of the incident beam at the sample, allowing the user to increase the pulse peak power and preserve the average pulse power over the duty cycle period[13]. The increase in pulse peak power is particularly significant within CARS excitation due to the event's signal generation having a direct quadratic relationship with the pump beam intensity. The increase in signal intensity achieved allows epi-direction signal detection with relatively low input power.

Unintrusive sample containment also manifested significant inhibitions to research progression, with sample plate manufactured flatness and strain contributing greatly to the ability to properly image separate wells within a single imaging cycle. After the exhaustion of market options, we turned to constructing the apparatus in-house using a silicone elastomer to attach each slide to a bottomless micro-well plate. Furthermore, imaging software was developed to allow automatic adjustment of the z-axis throughout an imaging cycle, hyperspectral capabilities through

adjustments of a delay stage, and compartmentalization of the code to allow ease of future edits and functionality additions. Enabled by the pulse-picking technology and epi direction signal detection, this CARS platform is the pioneer of nonlinear microscopes for HCS and successfully enables hyperspectral data collection with high chemical selectivity while simultaneously rejecting the use of any label and supporting the use of an incubation chamber and micro-well plates to control the microenvironments of individual biological samples in each well.

CHAPTER 2. STIMULATED RAMAN SCATTERING FOR HCS

2.1 Discussion

The advantages that accompany SRS over CARS in regard to spectral data collection were key factors in the initial employment of the spectroscopic technique for the HCS microscope. SRS lacks both a nonresonant background and spectral distortions, which present difficulties to researchers when attempting to isolate the sample's signal from these extraneous noise contributors[6,7]. Methods have been developed to minimize or remove the contributions from these sources, but each requires a significantly increased complexity to the instrument or its data analysis pipeline[14,15,16]. Additionally, the narrow peak width and the signal's linear dependence on concentration provides greater multichannel capabilities and simplifies the spectral data analysis, respectively[6,7]. Figure 2.1 provides the schematic which was followed for the construction of the microscope. The establishment and functionality of a visible SRS microscope for label-free, hyperspectral HCS is subsequently described.

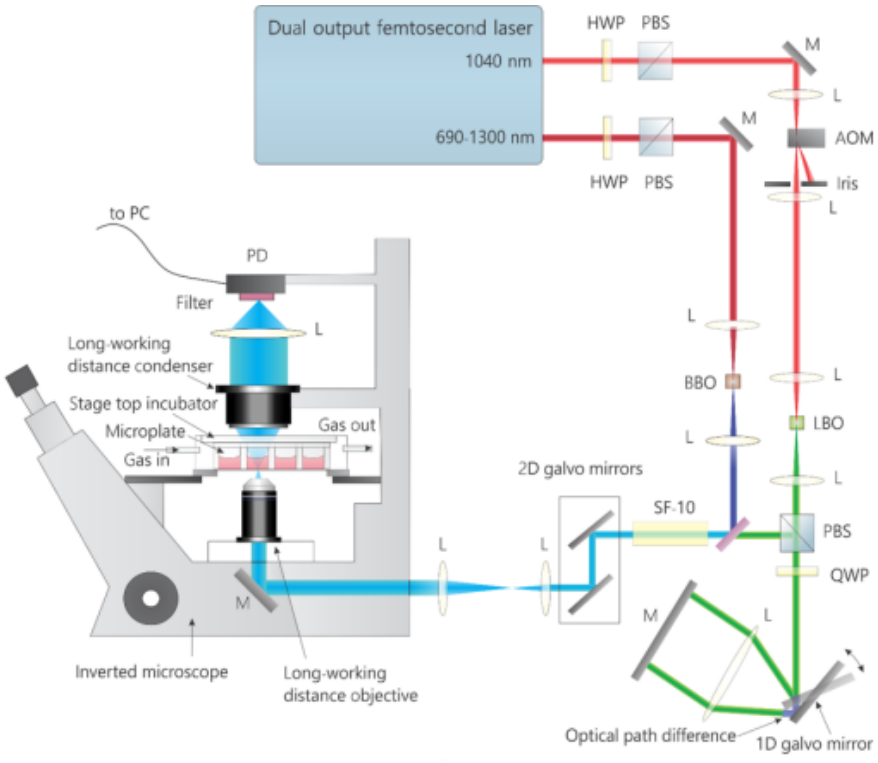

Figure 2.1. Schematic of inverted SRS microscope for HCS with 1D galvanometer mirror delay line for expedited hyperspectral imaging. HWP: Half-Wave Plate; PBS: Polarizing Beamsplitter; M: Mirror; AOM: Acoustic Optical Modulator; L: Lens; BBO: Beta Barium Borate crystal; LBO: Lithium Triborate crystal; SF-10: Glass rod for beam chirping; PD: Photodiode.

Modifications to the SRS platform from a standard configuration are unavoidable to retain the strong metabolic analysis capabilities of SRS for HCS. A tight focus at the sample plane of the pump and stokes beam is required to generate adequate signal levels, demanding the use of a high NA objective and significantly decreasing the working distance[7]. Furthermore, SRS is nonparametric coherent spectroscopy, with signal detection of the stokes carrier beam being performed in the forward direction[17]. Taken together, these characteristics inhibit the placement of common HCS hardware around the sample between the microscope's objective and condenser. Equipment such as micro-well plates or an incubation chamber become pipedreams for an SRS microscope if incident beam focus or complete signal collection cannot be achieved.

The resolution of the microscope *d* and NA of the objective is related through the equation $\boldsymbol{d = 0.61\lambda/NA}$, where λ is the wavelength of the incident beam[19]. To bypass the difficulties created from a short working distance, a lower NA objective was utilized. From the aforementioned equation for the resolution of the microscope, the wavelength of the beam at the sample must be appropriately adjusted to counterbalance the effects of the decreased NA objective. To remedy this dilemma, a BBO crystals were inserted in both the pump and stokes beam paths for frequency doubling. The result of this addition is a conversion of the pump and stokes beams to the visible range, 450 nm and 520 nm, respectively. The signal intensity of SRS is expressed in Equation 2.1[19]:

$$\Delta \boldsymbol{I_{SRS}} \propto \boldsymbol{Im}(\boldsymbol{\chi^{(3)}})\boldsymbol{I_P I_S} \qquad \textbf{(2.1)}$$

Where $\chi^{(3)}$ is the third order nonlinear susceptibility of the sample and I_P and I_S are the intensities of the pump and Stokes beams, respectively. The intensity of both the pump and Stokes beams have a linear relationship with the signal intensity. The total signal of SRS is proportional to its intensity, as determined from Equation 2.1, divided by the area of the laser focus, while the intensity is the average power divided by the beam size. Equation 2.2 relates the SRS signal to the beam size[19]:

$$\boldsymbol{P_{SRS}/A} \propto \boldsymbol{Im}(\boldsymbol{\chi^{(3))}})\boldsymbol{P_P\, P_S/A^2} \qquad \textbf{(2.2)}$$

Through the process of frequency doubling, both the wavelength and beam size are halved, resulting in a doubling of the total SRS signal P_{SRS}. The use of a shorter wavelength additionally yields higher signal levels through pre-resonance enhancement for certain molecules.

To achieve hyperspectral imaging, or the collection of a full spectrum at each pixel to be used for more discrete sample analysis, a 1D galvanometer mirror (1D galvo) is installed in the Stokes line to provide an adjustable delay of the beam[20]. Figure 2.2 illustrates this 1D galvo delay setup. The incremental adjustment of the 1D galvo with respect to sample scanning creates a time delay of Δt for a Stokes pulse which is expressed in Equation 2.3, where Δx is the additional distance traveled by the Stokes beam due to the rotation of the 1D galvo. The biased delay of the Stokes pulses allows us to spatially tune their alignment with corresponding probe pulses.

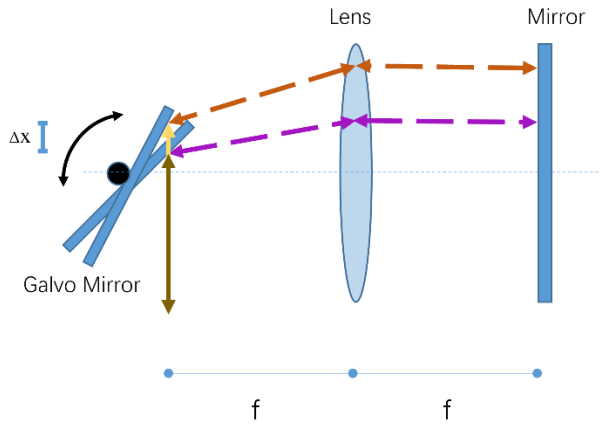

Figure 2.2. Schematic of 1D galvanometer mirror micro-delay line for the Stokes beam. Spatial delay of beam is two times the additional distance it must travel to the galvanometer, represented by Δx, before deflected to the central lens, as the same path is traveled again after reflection on the mirror.

$$\Delta t = \frac{\Delta x}{c} \qquad (2.3)$$

The abovementioned visible SRS microscope was successfully constructed and the resolution and sensitivity were evaluated. To actualize the platform's HCS capabilities, micro-plates are used to analyze concentration gradients of drug or metabolic permutations in biological samples. An incubation chamber is also installed surrounding the microplates to maintain and adjust the temperature, O_2 concentrations, and CO_2 concentrations of the sample environment in real time[21,22,23]. These inclusions allow for a thorough approach to understanding how multiple parameters of a sample are impacted by varied access to chemical additives and to manipulate the sample's environment to resemble *in vivo* conditions more closely. Drug combinations can be

examined to determine if a given pair provides additional benefits to treatment through additive effects or if new side effects need to be considered for patients prescribed both substances. Using the incubation chamber, an environment such as the hypoxia conditions created in the center of tumors can be mimicked and explored[22,23]. This design presents an attractive platform for HCS to researchers in biology and pharmaceuticals, maintaining chemical selectivity in label-free imaging in addition to a robust agency in experimental design.

2.2 Results

SRS signal acquisition is in the forward direction using a photodiode after passing only the Stokes signal carrier beam with a 500 nm high pass filter. An AOM is used to modulate the Stokes beam so that demodulation of the detected signal with a lock-in amplifier leads to the determination of the Raman shift through the nonparametric SRS event[23]. A DMSO droplet housed between two glass slides for measurement by cutting the center out of a piece of double-sided tape was used for signal optimization and signal-to-noise calculation. The droplet sits in the central cutout of the double-sided tape while the remaining outer ring of the tape binds to the glass slides. Figure 2.3 depicts the containment structure for the DMSO droplet, as well as the SRS image generated when viewing the edge of the droplet. The signal-to-noise ratio (SNR) of the SRS signal can be calculated using equation 2.4:

$$\boldsymbol{SNR = \frac{Mean_{Signal} - Mean_{Noise}}{\sigma_{Noise}}} \qquad \textbf{(2.4)}$$

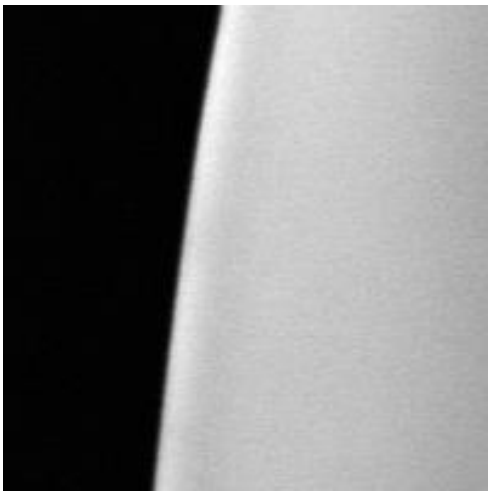

Figure 2.3. SRS image of edge of DMSO droplet. This field of view allows the sample signal-to-noise ratio to be calculated. The SNR for the SRS microscope was calculated to be 120.00 for a pure DMSO droplet with pump power at 4.3 mW and Stokes power at 16.1 mW.

The SNR for this platform was calculated to be 120.00 using the droplet's SRS signal in Figure 2.3. The powers used were 4.3 mW and 16.1 mW for the pump and Stokes beams, respectively. The SNR was not calculated in a heterogenous sample, such as cancerous tissue that the platform is designed to analyze, due to the difficulty in homogenizing the signal in these complex samples and sorting sources of signal from noise. This metric is in line with other SRS high-resolution techniques. For resolution determination, the full-width half-max (FWHM) of the smallest measurable particle size within an image of Mia PaCa-2 cells is calculated using the curve fitting function in Origin, as illustrated in Figure 2.4, where the FWHM is found to be 2.62. This yields a resolution of 262 nm, from a pixel size of 100 nm. With the exchange of a low NA objective and visible excitation pulses, the SNR is much lower than conventional SRS imaging. Therefore, the decision was made to transition to a high-NA objective lens for imaging biological samples.

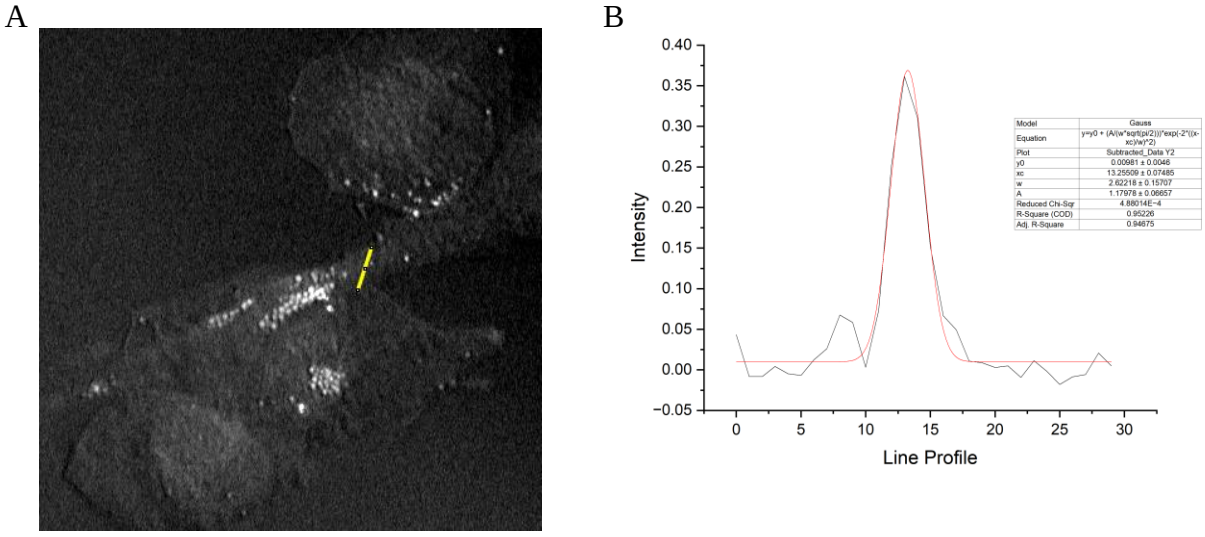

Figure 2.4. (A) SRS image of Mia PaCa-2 cells with yellow line overlay of a lipid droplet. Pixel diameter is approximately 100 nm. (B) Line spectrum of the overlay with Gaussian curve fitting. FWHM is 2.62, leading to a resolution of 262 nm.

With the total energy input to the sample having direct impacts on signal intensity, as can be extrapolated through Equation 2.1, repetitive imaging of a sample demands a balance between energy input to support high resolution and averting photodamage, which evolves from this same sustained high energy input to the detriment of sample analysis. Photodamage is the burning and

degradation of a sample and prevents any beneficial metabolic analysis which could subsequently be made. Figure 2.5 is an example of photodamage progression in cells while testing the incident power limitations of the visible SRS, with pump and Stokes powers at the sample being 10 mW and 10 mW, respectively. Panel A and B are the same images displayed using different contrast ranges. Panel A shows cells and the lipid droplets within them, while panel B, through contrast adjustment, highlights several bright spots with much stronger intensity. These spots are attributed to the plasma and white light generated during the photodamage of the samples. Since the beam focuses are much smaller using a visible beam compared to IR, as well as the higher photon energy at shorter wavelength, even at a lower excitation average power than the IR laser excitation, visible SRS has a higher proclivity of inducing photodamage in biological samples.

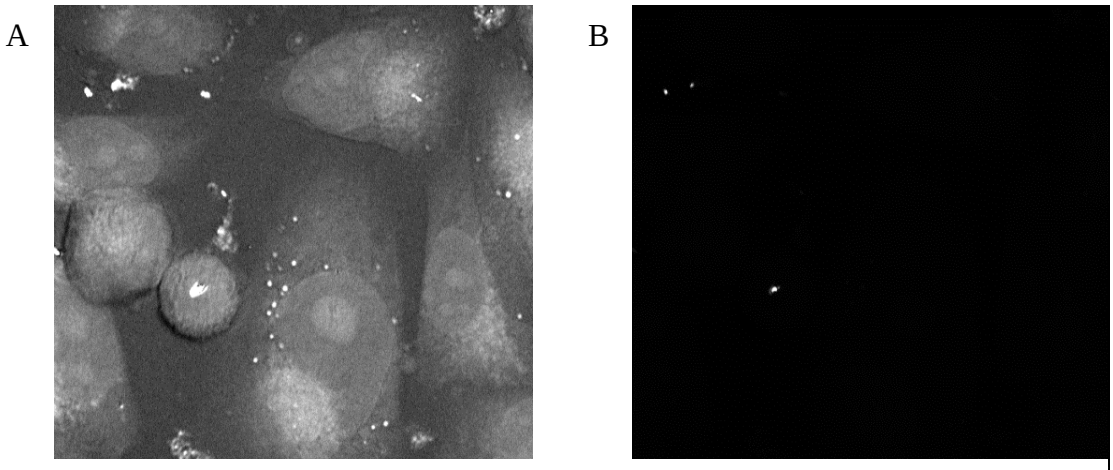

Figure 2.5. (A) A visible SRS image of MIA PaCa2 cells using 10 mW pump beam and 10 mW Stokes beam with a 10 microsecond pixel dwell time exposure. (B) Changing the contrast in A to display the white light-generating spots, indicating the photodamage to the sample.

The balance between signal generation and averting photodamage proved a bane for the visible SRS screening of biological samples, as SNR saw a drastic drop at the low powers necessary to retain sample integrity. Through many iterations of imaging parameters, such as pulse power, pixel dwell time, and pixel size, an adequate solution was not able to be reached for eliminating photodamage while generating sufficient signals from cells.

2.3 Conclusion

The development of this visible SRS microscope provided integral information for successfully constructing a nonlinear, label-free HCS platform. The standards required of the system left no room for the appearance of photodamage throughout imaging. Furthermore, consecutive screening of the same sample is an imperative capability of a marketable system desiring to replicate *in vivo* environments and provide real-time metabolic information, wherein the measurable change of metabolism can provide valuable insight into drug functionality or chemical pathways. Despite this pitfall, the visible SRS pipeline was not scrapped, and deliberation began to determine new applications and/or modifications that may again justify the resources already devoted to it. Visible SRS can provide insight into the crystalline structure and properties, with samples relevant to this type of data collection coincidentally having a considerably higher tolerance to the power of an incident pulse. One such category of samples is non-biological samples such as pharmaceutical ingredients in drugs, where the system can become a valuable tool in the industry's arsenal for R&D and quality control. The high chemical selectivity and resolution of the method coupled with the greater working distance achieved could lead to innovations in fields requiring quick image or spectral analysis, especially those demanding high throughput of samples.

CHAPTER 3. PULSE-PICKING CARS FOR HCS

3.1 Discussion

As the SRS line was placed in hibernation for later development in low wavenumber spectroscopy, the assessment of the HCS project began with the determination of what necessary considerations and modifications would be needed to enable its intended functionality when converted into a CARS platform. CARS is a parametric process, meaning the event does not contribute to energy transfers to the molecular system[5]. A pulse-picking method developed by Matthew Clark et al. using an acousto-optic modulator (AOM) is also employed in this iteration to take advantage of its ability as an optical chopper of high energy pulses to increase signal generation with a low average pulse input power[13].

Certain undesirable characteristics of the CARS excitation process, not found in the previously administered SRS process, must be tolerated and/or nullified to maintain the image and spectral fidelity. Signal generation in CARS is dependent on a quadratic relationship with both the intensity of the incident probe pulse, I_P, and the third-order nonlinear optical susceptibility of the sample, $\chi^{(3)}$, as represented by equation 3.1[7]:

$$\boldsymbol{I_{CARS} \propto |\chi^{(3)}|^2 I_P^2 I_S} \qquad \textbf{(3.1)}$$

These relationships result in a hindrance to the processing of the collected signal, wherein it becomes more difficult compared to referencing a linear relationship to untangle and isolate the contributions provided by each variable for the signal intensity. The most significant detractor for CARS imaging is the constant presence of a nonresonant background (NRB). Equation 3.1 describes how the NRB distorts a CARS spectrum:

$$\boldsymbol{\chi^{(3)} = \chi_R^{(3)} + \chi_{NR}^{(3)}} \qquad \textbf{(3.2)}$$

Many processes, such as the near-resonance phenomena and four-wave mixing process, can contribute to this background which is intrinsically linked with the coherent anti-Stokes field, making its compensation or removal a challenging task.

Numerous approaches have been explored to address the continuous bane of the NRB, such as using signal separation, like those capitalizing on the polarization difference between the CARS

resonant signal and the NRB, or background compensation techniques, such as machine learning tools trained to recognize and remove the NRB, or pulse shaping methodologies to create a destructive interference to nullify the NRB[24,25,26,27]. However, all these approaches function off the assumed necessity of sufficient signal generation for single cells, which is typically achieved via forward-direction signal acquisition. As discussed in Chapter 2, such a forward detection scheme is incompatible with HCS. Instead, epi-CARS signal detection can be considered as a viable alternative for HCS platforms, which simultaneously suppresses the NRB. However, epi-CARS suffers from a weaker signal generation, so a pulse-picking method is implemented to allow the generation of strong CARS signals, even in the epi-direction, with low input average power for excitation. Figure 3.1 is the schematic of our developed microscope to support HCS using CARS, featuring an alternatively purposed AOM for pulse picking compared to that used in the SRS microscope for signal reference.

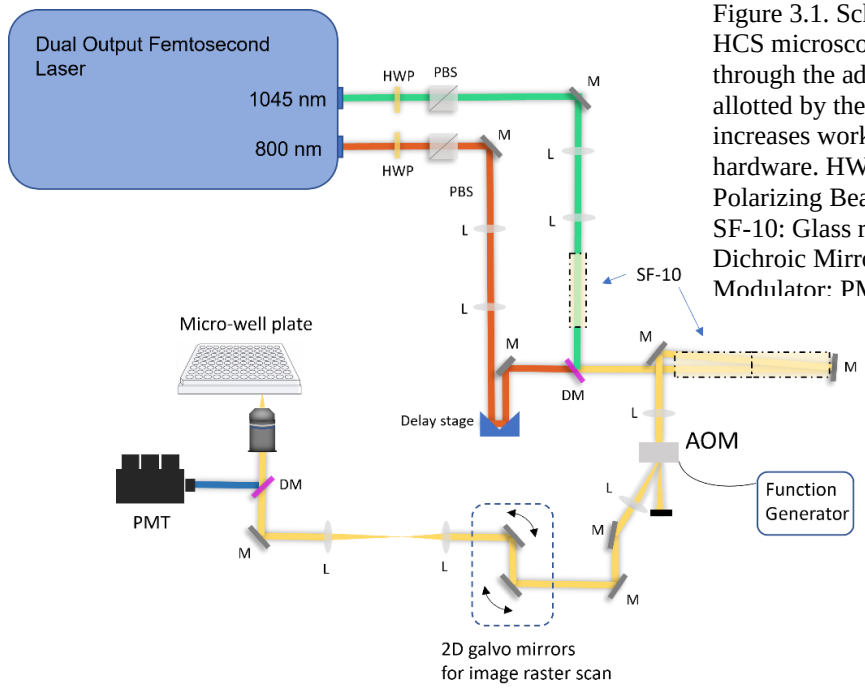

Figure 3.1. Schematic of inverted PP-CARS HCS microscope. Inversion supported through the additional epi-direction signal allotted by the pulse-picking technology and increases working distance for HCS hardware. HWP: Half-Wave Plate; PBS: Polarizing Beamsplitter; M: Mirror; L: Lens; SF-10: Glass rods for beam chirping; DM: Dichroic Mirror; AOM: Acoustic Optic Modulator; PMT: Photomultiplier Tube.

This label-free, pulse-picking CARS (PP-CARS) microscope relies on a pulse-picking technique using an AOM to increase system sensitivity and enable epi-direction CARS signal without using an excessive amount of power or sacrificing the imaging speed.

3.1.1 Pulse-Picking CARS and Epi-Direction Signal Collection

PP-CARS relies on an AOM to act as an optical chopper of both the pump and Stokes beams[13]. The consequence of such an interruption in the beam path is the ability to decouple pulse-peak power from the average power at the sample. With nonlinear methods, such as CARS, this endeavor becomes quite enticing for maximizing signal generation, on account of the signal intensity's direct relationships with the pump and Stokes intensities, and mitigating the photodamage a sample incurs, which is intrinsic to the excessive average power input to the sample over a given exposure time[7]. Figure 3.2 illustrates how picking pulses can allow for an increase in the pulse peak power without affecting the average power.

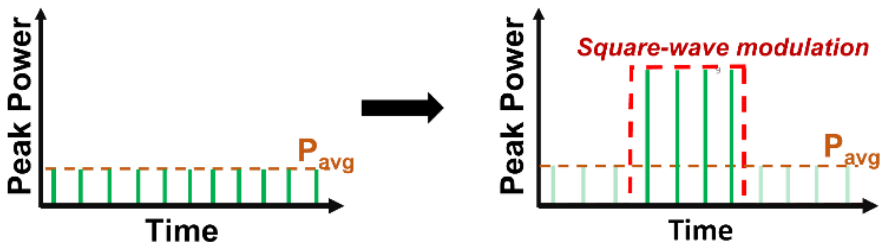

Figure 3.2. The theory underlying the pulse-picking technology. Pulse peak power is increased, but an AOM selects only a percentage of pulses in a given pulse train (described by the duty cycle) to maintain the same average input energy to the sample. The CARS signal increases with the pulse peak power to allow epi-direction imaging and photodamage is limited without the average input power also increasing[13]

The number of pulses selected for a time period is represented and set through the function generator's duty cycle, which regulates the percent of a time cycle the AOM is active[28]. When inactive, the AOM simply allows any pulses to pass through and yields the zeroth order beam bath. For this particular configuration, the zeroth order path is safely removed using a beam dump. For active periods in a cycle, an acoustic wave is passed through the AOM's crystal to manipulate its refractive index. Pulses passing through the AOM during this period will have their trajectory

appropriately adjusted, implementing first-order diffraction. Tuned correctly, the spatial overlap of the pump and Stokes beams can be maintained, despite their disparity in wavelength. The first-order diffraction of the AOM is finally routed to the sample for imaging.

If a 100% duty cycle has a given average power assigned to it, then it follows that a user may reduce the duty cycle to increase the pulse peak power without altering the original average power. Due to the relationship between signal intensity and incident beam intensity, we are able to dramatically increase the sensitivity (approximately 1,000x) of CARS imaging through the pulse-picking technique at the same input average power. Figure 3.3 demonstrates the drastic forward and epi-direction image quality increase accomplished with a pulse-picking duty cycle of 1.4% and how it favorably compares to non-pulse-picking signal detection (97% duty cycle)[13].

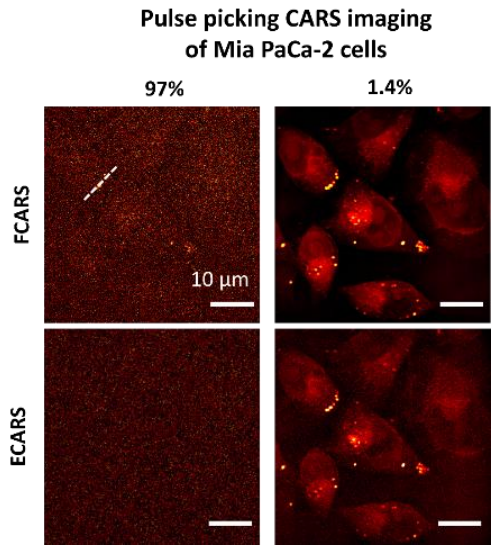

Figure 3.3. Direct comparison of forward- and epi-direction CARS microscopy image quality at constant pump and Stokes powers through application of the pulse-picking technology. The sensitivity increase from pulse-picking allows the epi-direction CARS to be manageable for modern image analysis and to circumnavigate the common pitfalls of forward-direction detection for nonlinear techniques in HCS[13].

This unprecedented sensitivity increase allows for the HCS system to achieve high-resolution imaging using epi-direction CARS. Epi-direction signal detection reduces the coherent NRB and alleviates the need to consider the detrimental effects the HCS sample containment hardware may have on imaging capabilities.

3.1.2 Imaging Software

To facilitate HCS, imaging software was developed in tandem with the Jonathan Amy Facility for Chemical Instrumentation (JAFCI) at Purdue University. The software is designed to

support ever-evolving, multi-modal imaging platforms. Using LABVIEW, the software is segmented into separate protocols and parameters set by the user to instruct the software on how to call the protocols throughout imaging a sample. This creates a considerably more mutable framework compared to codes with no separation of their parts. Adjustments and additions to the software are simplified where one must isolate the region where changes are to take place. Once a protocol is changed or created, the edit is reflected in the governing code-calling protocols. The governing portion of the code is written in a manner that enables the user to control the order and/or ratio in which protocols are called, broadening the number of modes the microscope can support and increasing the number of sample containment platforms it can accommodate.

Priority was also placed on the creation of a user-friendly interface for the software, to accommodate many scientists who may not be intimately familiar with the microscope's function or possess identical goals during its use. Figure 3.4 shows the software's different interfaces where a user sets parameters for an imaging sequence and can monitor the field of view in real-time. Below the image window is a graph where line spectra of line profiles across the image can be monitored. The first tab is for configuration with the inputs and outputs the software is to communicate with and contains some parameters for the system which must be preset, such as hyperspectral stage step size and units. Connections include: scanning galvanometer ports, the data acquisition channel of the detector to be used, and both the microscope and hyperspectral stage control ports. The second tab is to establish image parameters. The user may choose to receive a continuous feed or snapshots of the field of view and can make adjustments to it for optimal data collection, such as the hyperspectral delay to change the initial vibrational frequency being targeted for excitation, number of pixels being imaged in the x and y dimensions, and the image span, which relates to the size of pixels and the distance imaged in the x and y dimensions. The "Pre-Line pts" and "Post-Line pts" are important settings that tell the software how many pixels to remove at each end of individual scan lines performed by the galvanometers. At the tail ends of these lines the mirrors do not have constant velocities and, if the corresponding pixels are not removed, the resulting image will be blurred across these areas. One may also select the sampling frequency, starting corner of the sample plate, and the type of raster scan, either a unidirectional or bidirectional raster.

The third and final tab predominantly pertains to the incremental parameters which will be used during the scanning process for HCS. A "Home" position is first set and denotes the starting

point for each scan. The user may change this set position any number of times and return to it using the “Go Home” command when exploring other areas of the sample. The use of a minor step during scanning, in addition to the required major step, may be toggled here. The major step corresponds to the movement between wells and the minor step to the movement within a single well to increase sampling. For both the major and minor steps, the number of steps being performed and their sizes can be set for the x, y, and z dimensions. Steps in the x and y dimensions pertain to the field of view relative to the sample plane, whereas those in the z dimension are used to maintain image focus as the platform samples between wells. However, this is only able to account for consistent z-dimension shifts and is not capable of auto-focusing. The ability to perform hyperspectral imaging is toggled on this tab. This process is managed by a delay stage for the pump beam which changes its alignment with the Stokes beam to change the wavenumber being targeted. One may change its starting point, step size, and the number of steps to be taken at each pixel. Finally, a file path is created and designated for the software to save the data to. Filenames for each well are assigned which denote its coordinate within the sample plate.

The development of this software has greatly improved the efficiency and control of imaging through its straightforward interface. In a lab focused on imaging technology and method development, the ease of incorporating new or improving imaging modes into the software for it to facilitate is highly desirable and alleviates the burden of the microscopist usually associated with this task.

A

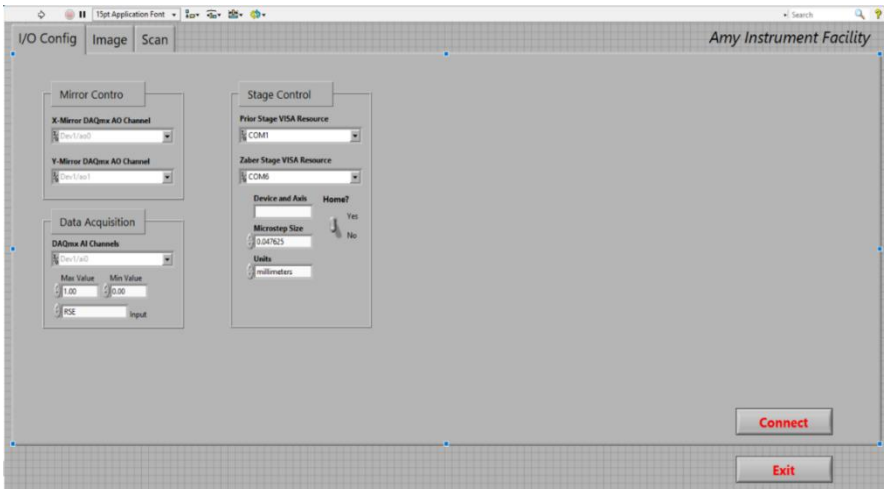

B.

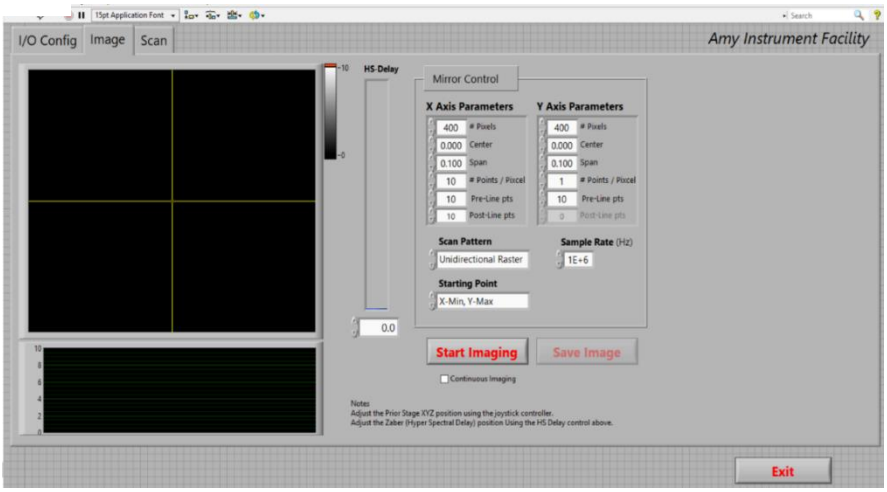

C.

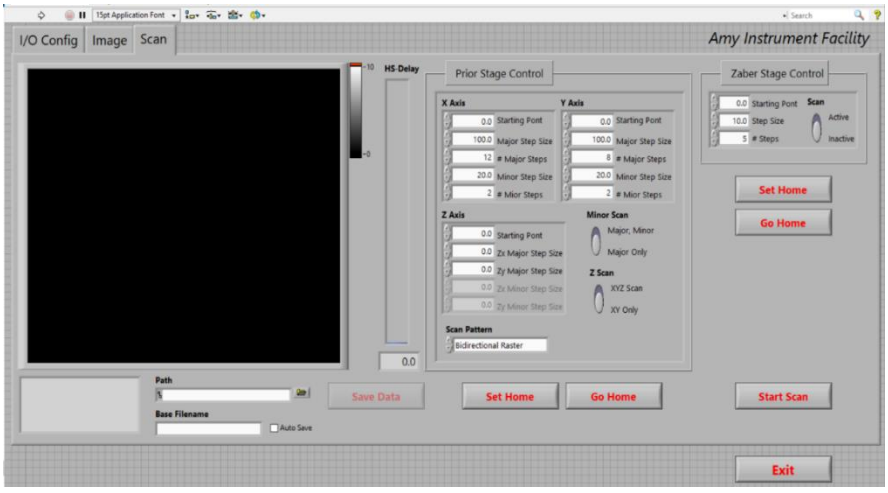

Figure 3.4. Interfaces for Imaging Software. (A) Configuration tab to establish connections between the software and hardware and to set some hardware parameters before imaging. (B) Sets image dimensional and quality parameters with continuous imaging capability. Microscope field of view and line profiles across the image are presented on the left of the tab. (C) Rightmost window displays image for each major step scan. Middle window sets and runs programmed imaging sequence, with major and minor step size and number in the x, y, and z dimensions. Top right window toggles and controls hyperspectral capabilities. Bottom of window manages saving data and home position of microscope stage.

3.1.3 Sample Containment

Many iterations for sample containment have been tested to find a setup that seamlessly integrates within the HCS platform. The novelty of the microscope detrimentally affects the ability to ascertain a market option for sample containment whcih functions as required. Originally, a common 96-well micro-plate, pictured in Figure 3.5, was considered suitable for the project[29].

Figure 3.5. 96-well micro-plate with 170 μm bottom slide thickness. Provides a versatile platform for HCS experiments on biological samples[29]. The relatively small slide thickness resulted in warping of its surface and the inability for focus on the sample plane to be preserved from well to well[29].

However, the use of epi-direction imaging of microplates compounds the necessary focus shift from changes to the sample slide height, as the height change is now represented twice in the path of the incident beam to the detector. The tight focusing requires the sample plane to be well-maintained when scanning between wells. The standard 170 μm thickness of these slides prevented meaningful use of the microscope for HCS, as moving the field of view outside a single well would shift its sensitive focus beyond usable limits. Figure 3.6 reveals the cause and solution discovered to prevent the erratic shift of the focus between wells. The manufacturing process for 170 μm slides permits warping of the surface[30]. Compare this to 1 mm thick slides, where only a constant slope across the slide surface is present after gravity causes the surface to settle. It was found that a separate z-dimension step for the x- and y-dimensions was satisfactory during imaging to retain focus on the sample plane. Capitalizing on the segmented form of the imaging software, this was not a difficult protocol to implement.

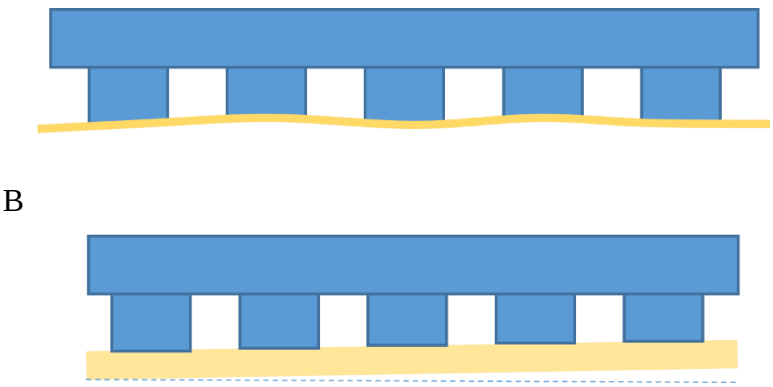

Figure 3.6. Comparison of sample slide (yellow) flatness variation according to its thickness. (A) 170 μm thick slide causing warp of slide surface. (B) 1 mm thick slide with constant slope relative to microscope stage plane.

Any sample plate must also not interfere with the functions of the incubation chamber. Many plates were deemed incompatible with the dimensional restrictions of the incubation chamber and/or failing to maintain the air-tight seal around the sample. Figure 3.7 depicts a product manufactured by Grace Bio-Labs called ProPlates which relied on clamps along its edge to secure the slide to the chambers[31]. After reducing the warping of the slide caused by the force of the clamps, it was found that gaps propped up by the clamps remained in between the plates and the incubation chamber walls. It was decided that solutions to these gaps decreased the useability and throughput of the HCS platform and that continued exploration of sample containment options held greater promise.

Figure 3.7. Grace Bio-Labs ProPlate for HCS sample containment. Utilizes clamps on outer edge to hold the slide to the bottomless plate[31]. Slide warping can be relieved by reducing clamp force. Uneven surface created by the clamps causes gaps in incubation chamber seal[31].

Two structures found to-date have the capability of working in the HCS platform. The first, shown in Figure 3.8, is produced by Ibidi and advertises a bottomless plate with an adhesive surface for sticking to a slide, though this design can be found at other manufacturers[32]. They are bottomless silicone chambers that use an adhesive for attachment to the glass slide and lack the force to warp the glass surface. Using a plasma cleaner, this structure can be sanitized without deteriorating the adhesive. However, thin-walled bottomless adhesive chambers were found to have reduced effectiveness for proper sample containment, with leaking or contamination between adjacent wells becoming likely. The possibility of long storage/incubation periods and multiple rounds of imaging means confidence must be high that a given sample remains unblemished throughout, lest a resource-intensive experiment fails to deliver constructive data and must be repeated. Therefore, the size and number of wells are limited for this containment variant, where chambers with greater than twenty wells express high rates of failure.

Figure 3.8. Ibidi sticky 18-well bottomless plate. Compatible with 1 mm thick slides[32]. Adhesive interactions with the slide are inconducive to the slide's natural surface topography[32].

After exhausting market options, a carefully constructed in-lab structure was pursued. Appearing almost indistinguishable from a traditional 96-well micro-plate, individual components were prudently sourced and then assembled by hand. A large, 1 mm thick glass slide is first cut to size and Sylgard 184, a silicone-based elastomer, is used to adhere it to the surface of a bottomless 96-well micro-plate. Steady hands, a level and liberal application of elastomer, and the use of a support apparatus to stop slippage of the slide during drying were found to be paramount in producing the intended, high-quality sample chamber. If the slide moves throughout any point of this process across the plate, the elastomer will cover its surface and prevent cell growth and imaging over those areas. When too little elastomer is deposited across the back of the bottomless

plate, then significant pressure is required to form a seal between the plate and slide and causing inadvertent warping of the slide surface after the elastomer has cured. Due to temperature sensitivity, sterilization must be accomplished using a plasma cleaner rather than an autoclave. Once properly assembled, the apparatus meets each qualification required of it to enable HCS of treated biological samples in a controlled environment without becoming a nuisance for either the CARS excitation process or microscope focus.

3.2 Results

Epi-direction signal detection is accomplished using a photo-multiplier tube (PMT). A 500 nm high-pass filter is used to reduce photo-contamination from superfluous sources. After temporal and spatial alignment and optimization of the pump and Stokes beams, spectral characterization and sensitivity measurements of the platform ensued. Dimethyl sulfoxide (DMSO) droplets were measured because of their well-established CARS spectral response[33,34]. Containment of the DMSO droplets was again done by sandwiching two glass slides together with a piece of double-sided tape and having its center removed. Figure 3.9 displays the DMSO spectrum as measured by the epi-CARS signal with spectral fitting.

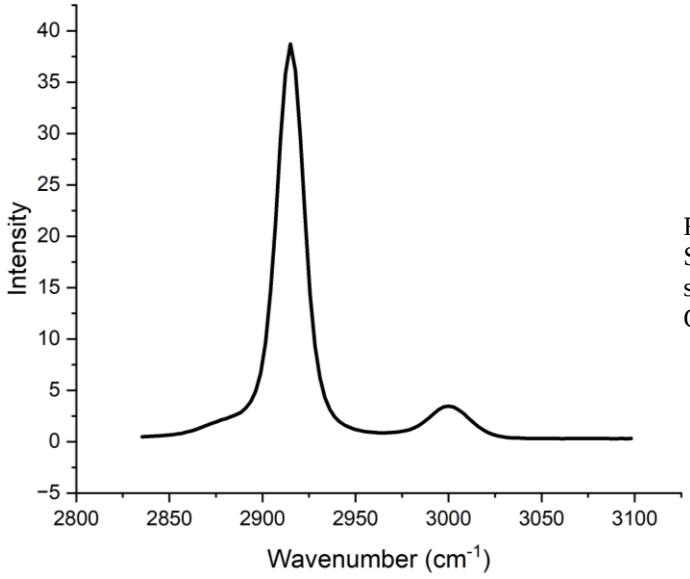

Figure 3.9. PP-CARS spectrum of DMSO. Signature peaks of the CH_3 symmetric stretching peak at 2915 cm^{-1} and asymmetric C-H stretch at 3000 cm^{-1}.

Sensitivity measurements consisted of gradual decreases in DMSO concentrations until the DMSO peaks could not be discerned from those contributed by the deuterium oxide (D_2O). The power for the pump beam was 11 mW and the Stokes was 13mW. Figure 3.10 contrasts the 0.1% DMSO spectrum with the pure D_2O spectrum, in which the DMSO peak around 2915 cm^{-1} can still be observed above the baseline noise within the phase-retrieved Raman spectrum of 0.1% DMSO using Kramer-Kronig relations with the pure DMSO.

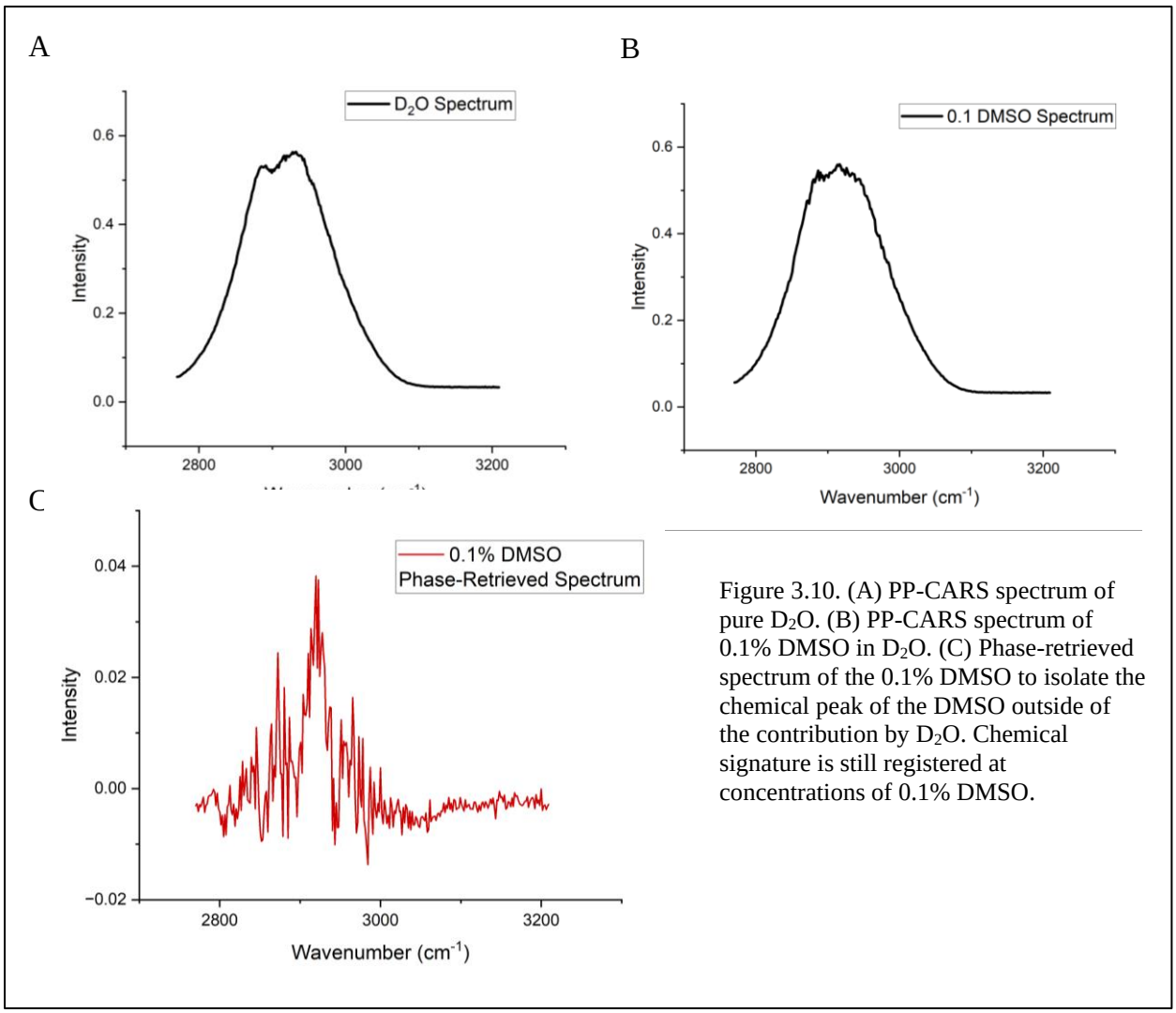

Figure 3.10. (A) PP-CARS spectrum of pure D_2O. (B) PP-CARS spectrum of 0.1% DMSO in D_2O. (C) Phase-retrieved spectrum of the 0.1% DMSO to isolate the chemical peak of the DMSO outside of the contribution by D_2O. Chemical signature is still registered at concentrations of 0.1% DMSO.

Due to the difficult task of unraveling the complex contributions from a heterogeneous sample to spectral signals, SNR is more appropriately reported using a homogenous DMSO droplet. Figure 3.11 is an image at the edge of the DMSO droplet used for SNR determination. The SNR was calculated to be 154.32 for the platform from the droplet's signal using Equation 2.4. Both the pump and Stokes beams were at 10 mW for this measurement.

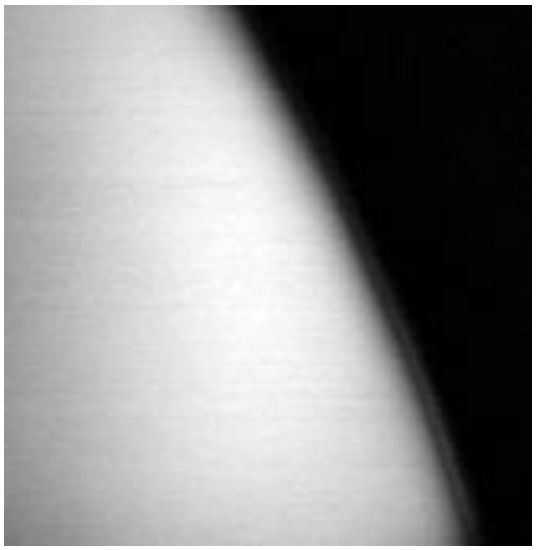

Figure 3.11. Border of DMSO droplet. SNR is calculated using Equation 2.4 to be 154.32. Pump and Stokes powers are each 10 mW.

The resolution of the PP-CARS microscope was ascertained from the FWHM of the spectral peak of the smallest measurable feature in a Mia PaCa-2 cell. Figure 3.12 displays the cell with the spectral line overlapping the selected feature to determine the resolution and the subsequent spectrum created with the Origin calculation of the FWHM. The resolution is found to be approximately 270 nm, from a FWHM of 2.57 and pixel size of 105 nm.

A

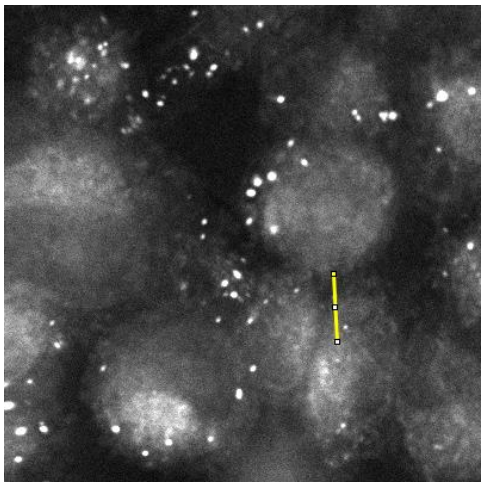

B

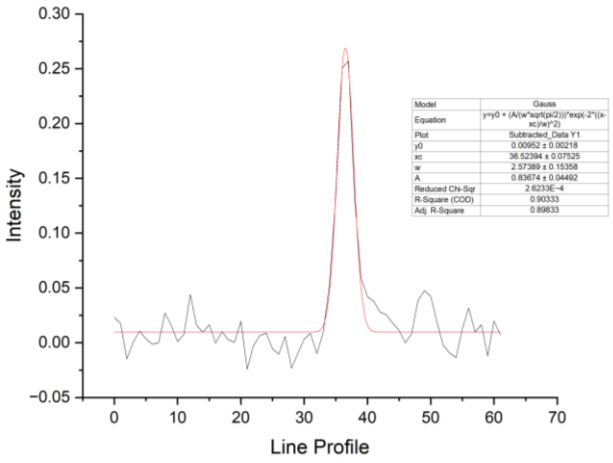

Figure 3.12. (A) Mia PaCa-2 cells for measurement of a spectrum over a small lipid droplet feature across the yellow line. (B) The spectrum of the line profile with an FWHM of the lipid droplet peak of 2.57. The resolution is thus 267 nm with a pixel size of 105 nm.

The imaging software has been thoroughly tested for its communication with the microscope, specifically for proper sample stage programming and control, and found to replicate designated imaging protocols. Success has also been found with the incubation chamber for the replication of hypoxia environments that would be found at the centers of tumors, with Figure 3.13 contrasting Mia PaCa-2 cells incubated in normoxia and hypoxia conditions with the incubation chamber. Lipid droplet formation can notably be observed to transition in greater concentrations to the endoplasmic reticulum in the hypoxia sample, which is hypothesized to reduce the stress experienced by the endoplasmic reticulum from the abnormal conditions.

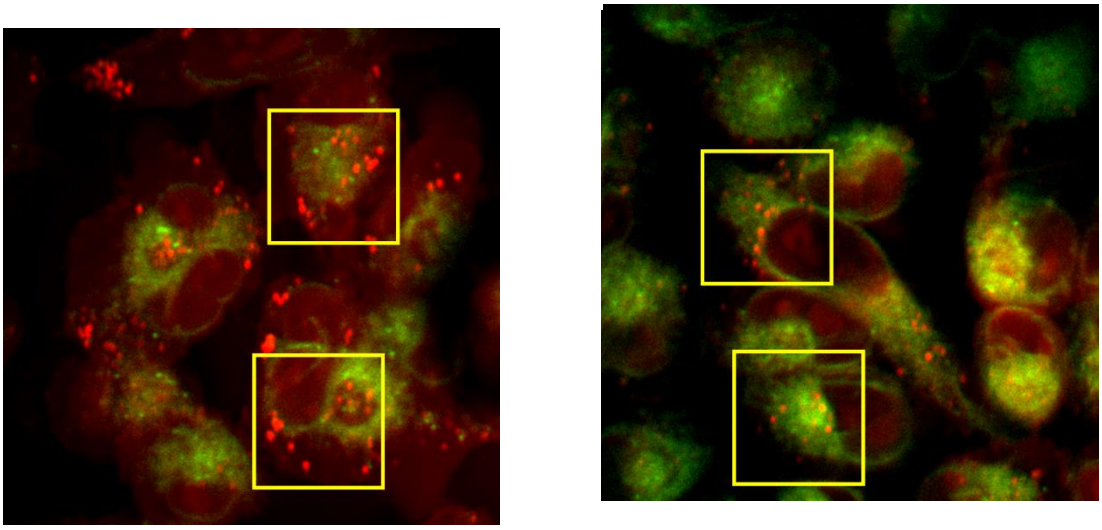

Figure 3.13. (A) Mia PaCa-2 incubated in normoxia conditions with lipid droplets scattered throughout the cell. (B) Mia PaCa-2 cells incubated in hypoxia conditions with lipid droplets concentrated in the endoplasmic reticulum as a stress response.

3.2.1 Experimental Demonstration of Label-Free Imaging and HCS

Proof of concept will be carried out through three experiments. The first two are designed to demonstrate the platform's capabilities in metabolomics and biopharmaceutical research. Concentration gradients of two metabolites and/or pharmaceuticals are established across the rows or columns of the plate to analyze their synergistic effects on the behavior and health of the sample. Lipid droplet formation and composition is a plentiful source of metabolic information and the strong resonant signals produced by lipids allow for high-fidelity measurements[35,36,37,38]. For the metabolomics experiment the contributions of glucose and FBS to MIA PaCa-2, a pancreatic cancer cell line, lipid droplets will be imaged and quantified using this HCS platform. The purpose of the experiment is to gain a nuanced understanding of cancer cell resource consumption and growth vectors. This will strengthen treatment efficacy through an emphasis on cancer's metabolic pathways and possible points of attack and the versatility of the platforms lends itself to the screening of other cancer variants in a similar fashion[39,40].

The biopharmaceutical experiment will be staged using two cancer drug variants. Their individual and cumulative effects on the sample will be analyzed, as well as the intricacies of their

intermingling in the system. In addition to lipid droplet analysis, the high sensitivity and chemical selectivity of the platform enable the detection of discreet alterations to the sample instigated by the drugs, which is integral for determining the side effects of a patient's prescription. Though not definitive, Mia PaCa-2 or HeLa, a cervical cancer cell line, cells will be used in this experiment due to the relatively thorough understanding of these lines that their longstanding spotlight in cancer research has provided[41,42,43]. This experiment represents a gateway for researchers to discern how two drugs may enhance or handicap one another and the consequences their simultaneous presence in a system can have. Medical practitioners must have competent guidance on drug-drug interactions, as a patient's medical needs may be beneficially or adversely impacted by unique behaviors which arise when two drugs are in contact with one another[44,45]. This HCS platform will give pharmaceutical companies ample data on drug-drug interactions and its high throughput propensity expands the number of scenarios that can be studied, leading to safer drug development and prescription practices.

The final experiment will consist of the time-lapse analysis of cancerous tissue in a hypoxic environment, replicating the environment at the centers of tumors after their outer growth restricts oxygen supply from the distanced blood vessels[23]. This will add to the understanding of the unique metabolism of these deep tumor regions and lead to possible breakthroughs for transporting or developing novel treatments targeting a portion of tumors that does not have the ease of access that nearby blood vessels would otherwise enable[46]. The experiment will additionally demonstrate the platform's environmental control capabilities for mimicry of *in vivo* conditions and practicality for analyzing incremental changes to a system in real-time. The versatility of the HCS platform supports many combinations of drugs/metabolites, samples, and environments for high resolution, chemically selective analysis, and its label-free nature removes a possible contributing factor to unintended sample behaviors and misattributed diagnosis of phenomena. Through this platform, researchers will be able to closely replicate a biological system and arrive at more accurate, data-driven conclusions.

3.3 Conclusion

The PP-CARS HCS microscope exemplifies a powerful, novel instrument capable of label-free imaging and hyperspectral data analysis through its high chemical selectivity and resolution of biological systems. The HCS platform provides a holistic chemical profile of the sample with a

detachment and efficiency that label-reliant methods are not able to accomplish. Avoiding the complex interactions that labeling a sample inherently introduces is valuable for accurately studying innate metabolic interactions and pathways of a system. Though pending full experimental testing, the platform's completed assessment thus far has revealed its competency in supplanting and competing with analogous techniques relied on for metabolic and pharmaceutical research. Auto-focusing technology is being explored for the improvement of well-to-well focus consistency, but many market options rely on the signal generated by a wavelength that would significantly interfere with the CARS signal. Therefore, an adjusted feedback mechanism based on a shifted wavelength must be established for auto-focusing technology to be integrated into this platform. The development of the PP-CARS HCS microscope is a significant contribution to high-throughput, chemically selective sampling which leaves a specimen unperturbed by any labeling molecules to better replicate *in vivo* studies.

REFERENCES

1. Zanella, F., Lorens, J. B., & Link, W. (2010). High content screening: seeing is believing. *Trends in biotechnology*, *28*(5), 237-245.

2. Usaj, M. M., Styles, E. B., Verster, A. J., Friesen, H., Boone, C., & Andrews, B. J. (2016). High-content screening for quantitative cell biology. *Trends in cell biology*, *26*(8), 598-611.

3. Abraham, V. C., Taylor, D. L., & Haskins, J. R. (2004). High content screening applied to large-scale cell biology. *Trends in biotechnology*, *22*(1), 15-22.

4. Cheng, J. X., & Xie, X. S. (2004). Coherent anti-Stokes Raman scattering microscopy: instrumentation, theory, and applications. *The Journal of Physical Chemistry B*, *108*(3), 827-840.

5. Evans, C. L.; Xie, X. S., Coherent anti-Stokes Raman scattering microscopy: chemical imaging for biology and medicine. *Annu. Rev. Anal. Chem.* 2008, *1*, 883-909.

6. Freudiger, C. W., Min, W., Saar, B. G., Lu, S., Holtom, G. R., He, C., ... & Xie, X. S. (2008). Label-free biomedical imaging with high sensitivity by stimulated Raman scattering microscopy. *Science*, *322*(5909), 1857-1861.

7. Zhang, C., Zhang, D., & Cheng, J. X. (2015). Coherent Raman scattering microscopy in biology and medicine. *Annual review of biomedical engineering*, *17*, 415-445.

8. *Broadband Coherent Raman microscopy for the identification of tumors*. Dipartimento di Fisica - Politecnico di Milano. (2021, September 27). Retrieved January 21, 2023, from https://www.fisi.polimi.it/en/teaching/students/thesis_available/54196

9. Müller, M., & Zumbusch, A. (2007). Coherent anti-Stokes Raman scattering microscopy. *ChemPhysChem*, *8*(15), 2156-2170.

10. Spek, A. L. (2009). Structure validation in chemical crystallography. *Acta Crystallographica Section D: Biological Crystallography*, *65*(2), 148-155.

11. Ferrari, A. C., & Basko, D. M. (2013). Raman spectroscopy as a versatile tool for studying the properties of graphene. *Nature Nanotechnology*, *8*(4), 235-246.

12. Gouadec, G., & Colomban, P. (2007). Raman Spectroscopy of nanomaterials: How spectra relate to disorder, particle size and mechanical properties. *Prog Crys*, *53*(1), 1-56.

13. Clark, M. G., Gonzalez, G. A., & Zhang, C. (2022). Pulse-Picking Multimodal Nonlinear Optical Microscopy. *Analytical Chemistry*, *94*(44), 15405-15414.

14. Volkmer, A., Book, L. D., Xie, X. S. Time-resolved coherent anti-Stokes Raman scattering microscopy: Imaging based on Raman free induction decay. Applied Physics Letters. 80 (9), 1505-1507 (2002).

15. Marks, D. L., Boppart, S. A. Nonlinear interferometric vibrational imaging. Physical Review Letters. 92 (12), 123905 (2004).

16. Ganikhanov, F., Evans, C. L., Saar, B. G., Xie, X. S. High-sensitivity vibrational imaging with frequency modulation coherent anti-Stokes Raman scattering (FM CARS) microscopy. Optics Letters. 31 (12), 1872-1874 (2006).

17. Min, W., Freudiger, C. W., Lu, S., Xie, X. S. Coherent nonlinear optical imaging: beyond fluorescence microscopy. Annual Review of Physical Chemistry. 62 (1), 507-530 (2011).

18. Maznev, A. A., & Wright, O. B. (2017). Upholding the diffraction limit in the focusing of light and sound. *Wave Motion*, *68*, 182-189.

19. Paschotta, D. R. (2022, September 23). *Optical intensity*. Optical intensity, explained by RP Photonics Encyclopedia; physics, radiometry, energy flux, light intensity, amplitude, electric field, Poynting vector. Retrieved January 21, 2023, from https://www.rp-photonics.com/optical_intensity.html

20. Liu, X., Cobb, M. J., & Li, X. (2004). Rapid scanning all-reflective optical delay line for real-time optical coherence tomography. Optics letters, 29(1), 80-82.

21. Guzmán-Soto, I., McTiernan, C., Gonzalez-Gomez, M., Ross, A., Gupta, K., Suuronen, E. J., ... & Alarcon, E. I. (2021). Mimicking biofilm formation and development: Recent progress in in vitro and in vivo biofilm models. *iScience*, *24*(5), 102443.

22. Bhattacharya, S., Calar, K., & de la Puente, P. (2020). Mimicking tumor hypoxia and tumor-immune interactions employing three-dimensional in vitro models. *Journal of Experimental & Clinical Cancer Research*, *39*(1), 1-16.

23. Hockel, M., & Vaupel, P. (2001). Tumor hypoxia: definitions and current clinical, biologic, and molecular aspects. *Journal of the National Cancer Institute*, *93*(4), 266-276.

24. Marks, D. L., & Boppart, S. A. (2004). Nonlinear interferometric vibrational imaging. *Physical review letters*, *92*(12), 123905.

25. Volkmer, A., Book, L. D., Xie, X. S. Time-resolved coherent anti-Stokes Raman scattering microscopy: Imaging based on Raman free induction decay. Applied Physics Letters. 80 (9), 1505-1507 (2002).

26. Ganikhanov, F., Evans, C. L., Saar, B. G., Xie, X. S. High-sensitivity vibrational imaging with frequency modulation coherent anti-Stokes Raman scattering (FM CARS) microscopy. Optics Letters. 31 (12), 1872-1874 (2006).

27. Eckbreth, A. C., & Hall, R. J. (1981). CARS concentration sensitivity with and without nonresonant background suppression.

28. Berg, N. J., & Lee, J. N. (1983). Acousto-optic signal processing: theory and implementation. *New York*, *2*.

29. *96 well black plate, non-treated surface, no lid, non-sterile, pack of 10*. Thermo Fisher Scientific - US. (n.d.). Retrieved January 21, 2023, from https://www.thermofisher.com/order/catalog/product/237108

30. Achintha, M. (2016). Sustainability of glass in construction. In *Sustainability of construction materials* (pp. 79-104). Woodhead Publishing.

31. *ProPlate® Multi-well Chambers*. Grace Bio-Labs. (2023, January 4). Retrieved January 21, 2023, from https://gracebio.com/product/proplate-multi-well-chambers-246855/

32. *Sticky-Slide 18 Well*. ibidi. (n.d.). Retrieved January 21, 2023, from https://ibidi.com/sticky-slides/238-sticky-slide-18-well.html

33. Downes, A., & Elfick, A. (2010). Raman spectroscopy and related techniques in biomedicine. *Sensors*, *10*(3), 1871-1889.

34. Cheng, J. X., & Xie, X. S. (2015). Vibrational spectroscopic imaging of living systems: An emerging platform for biology and medicine. *Science*, *350*(6264), aaa8870.

35. Xu, S., Zhang, X., & Liu, P. (2018). Lipid droplet proteins and metabolic diseases. *Biochimica et Biophysica Acta (BBA)-Molecular Basis of Disease*, *1864*(5), 1968-1983.

36. Dugail, I. (2014). Lysosome/lipid droplet interplay in metabolic diseases. *Biochimie*, *96*, 102-105.

37. Greenberg, A. S., Coleman, R. A., Kraemer, F. B., McManaman, J. L., Obin, M. S., Puri, V., ... & Mashek, D. G. (2011). The role of lipid droplets in metabolic disease in rodents and humans. *The Journal of clinical investigation*, *121*(6), 2102-2110.

38. Thiam, A. R., Farese Jr, R. V., & Walther, T. C. (2013). The biophysics and cell biology of lipid droplets. *Nature reviews Molecular cell biology*, *14*(12), 775-786.

39. Kalyanaraman, B. (2017). Teaching the basics of cancer metabolism: Developing antitumor strategies by exploiting the differences between normal and cancer cell metabolism. *Redox biology*, *12*, 833-842.

40. Vander Heiden, M. G. (2011). Targeting cancer metabolism: a therapeutic window opens. *Nature reviews Drug discovery*, *10*(9), 671-684.

41. Yunis, A. A., Arimura, G. K., & Russin, D. J. (1977). Human pancreatic carcinoma (MIA PaCa-2) in continuous culture: sensitivity to asparaginase. *International journal of cancer*, *19*(1), 128-135.

42. Deer, E. L., González-Hernández, J., Coursen, J. D., Shea, J. E., Ngatia, J., Scaife, C. L., ... & Mulvihill, S. J. (2010). Phenotype and genotype of pancreatic cancer cell lines. *Pancreas*, *39*(4), 425-435.

43. Nelson-Rees, W. A., Hunter, L., Darlington, G. J., & O'Brien, S. J. (1980). Characteristics of HeLa strains: permanent vs. variable features. *Cytogenetic and Genome Research*, *27*(4), 216-231.

44. Magro, L., Moretti, U., & Leone, R. (2012). Epidemiology and characteristics of adverse drug reactions caused by drug–drug interactions. *Expert opinion on drug safety*, *11*(1), 83-94.

45. Becker, M. L., Kallewaard, M., Caspers, P. W., Visser, L. E., Leufkens, H. G., & Stricker, B. H. (2007). Hospitalisations and emergency department visits due to drug–drug interactions: a literature review. *Pharmacoepidemiology and drug safety*, *16*(6), 641-651.

46. Walsh, J. C., Lebedev, A., Aten, E., Madsen, K., Marciano, L., & Kolb, H. C. (2014). The clinical importance of assessing tumor hypoxia: relationship of tumor hypoxia to prognosis and therapeutic opportunities. *Antioxidants & redox signaling*, *21*(10), 1516-1554.